Petroleum Science 23 (2026) 1625–1635

Contents lists available at ScienceDirect

Petroleum Science

journal homepage: www.keaipublishing.com/en/journals/petroleum-science

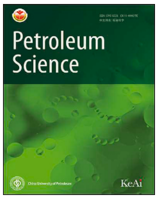

Original Paper

Effect of weak consolidation process of liquid bridge on interparticle mechanical behavior of clathrate hydrate

Qiang Luo [a], Zhi-Hui Liu [a], Xiao-Feng Dou [b], De-Li Gao [a,c], Zhi-Chao Liu [a,d], Fu-Long Ning [a,d,*]

[a] Faculty of Engineering, China University of Geosciences, Wuhan, 430074, Hubei, China
[b] Guangzhou Marine Geological Survey, China Geological Survey, Guangzhou, 511458, Guangdong, China
[c] MOE Key Laboratory of Petroleum Engineering, China University of Petroleum (Beijing), Beijing, 102249, China
[d] Institute for Advanced Marine Research, China University of Geosciences, Guangzhou, 511462, Guangdong, China

ARTICLE INFO

Article history:
Received 9 December 2024
Received in revised form
8 October 2025
Accepted 19 November 2025
Available online 22 November 2025

Edited by Xi Zhang and Jie Hao

Keywords:
Clathrate hydrate
Micromechanical force test
Liquid bridge
Hydrate shell
Consolidation

ABSTRACT

Clarifying the mechanism that results in the mechanical behavior differences of hydrate particles in different states is of great significance for understanding the agglomeration mechanism of hydrate particles and the mechanical behavior characteristics of the liquid bridge between particles in a pipeline environment dominated by oil or gas. In this study, the typical liquid bridge morphology and the consolidation characteristics of hydrate particles during the contact-pull process between hydrate particles and water droplets were observed using an improved micromechanical force testing device, as well as a force sensor with a higher sampling frequency and the electric displacement stage with a smaller step. It was found that the consolidation state of the liquid bridge changes in a complex manner in the gas phase environment, and there is a special weak consolidation state: when the hydrate shell on the surface of the liquid bridge is pulled off, a new hydrate shell will form on the surface of the unconverted water at the fracture until the liquid bridge is stretched to several times the particle diameter length and breaks. Based on the hydrate shell formation theory and the existing model of hydrate interparticle mechanics, a possible liquid bridge weak consolidation model was supplemented to explain this state to elucidate the mechanism that causes the difference in the mechanical behavior of the liquid bridge for hydrate particles in different states.

1. Introduction

Clathrate hydrate is an ice-like non-stoichiometric crystalline compound, in which water molecules form a space cage structure through a hydrogen bonding network and encase other molecules under certain temperature and pressure conditions (Sloan, 2003, 2004). Among them, methane hydrate is a solid formed by methane molecules and water molecules under low-temperature and high-pressure conditions. As a potential alternative energy source, methane hydrates occur widely in permafrost and marine environments. Numerous studies have shown that the amount of methane hydrates stored in the Earth may exceed the amount of known organic carbon sources (Collett et al., 2014). Hydrates have great energy potential and few environmental effects, however, they can cause damage in the conventional oil and gas industry, and there is a serious risk factor for the blockage of onshore and offshore oil and gas pipelines (Koh et al., 2011). When the water droplets in the pipeline are carried by natural gas, under suitable temperature and pressure conditions, hydrates begin to grow on the surface of the water droplets, and hydrate particles are formed from the hydrate shell. At the same time, the water droplets cause liquid bridge connections between the hydrate particles, and a large number of hydrate particles accumulate, leading to blockage of the pipeline (Delgado-Linares et al., 2013; Aman and Koh, 2016). Such blockage might also happen when the pipe surface has inhomogeneous chemistry caused by corrosions, contaminations, or even by soldering processes (Nguyen et al., 2020).

---

* Corresponding author.
E-mail address: nflzx@cug.edu.cn (F.-L. Ning).
Peer review under the responsibility of China University of Petroleum (Beijing).

https://doi.org/10.1016/j.petsci.2025.11.038
1995-8226/

To reveal the mechanism of pipeline blockage caused by hydrate agglomeration and adhesion, a large number of micromechanical force (MMF) tests and evaluation studies on hydrates have been carried out (Luo et al., 2024). Due to the strict temperature and pressure requirements for the formation of methane hydrates, the early MMF tests on hydrates were usually carried out on tetrahydrofuran (THF), cyclopentane (CP), and other hydrate samples that are easily formed under normal pressure. Yang et al. (2004) built an MMF test device for atmospheric hydrates with a temperature-controlled cell in an early stage, and they synthesized THF hydrate particles on the device to explore the effect of temperature on the mechanical behavior of THF hydrate particles. Taylor et al. (2007) improved Yang's work by adding a plexiglass chamber to reduce the influence of humidity and condensates on the testing process. Based on the test results, they proposed a theoretical shell forming model for hydrate particles formed by water droplets in the oil phase (Fig. 1). In this research stage, a large number of tests on the cohesion between hydrate particles and the adhesion between the particles and the material surface were carried out (Yang et al., 2004; Taylor et al., 2007; Dieker et al., 2009; Nicholas et al., 2009; Aspenes et al., 2010; Aman et al., 2010; Aman et al., 2012; Aman et al., 2012; Aman et al., 2013; Aman et al., 2014; Liu et al., 2015; Sato et al., 2016; Hu and Koh, 2017; Wang et al., 2020). Aman et al. (2011) proposed an interparticle mechanical calculation model for hydrates that considers liquid bridge consolidation based on the test results. Liu et al. (2017b) proposed a modified calculation model that considers the reduction of the volume of the liquid in the liquid bridge due to partial consolidation. Nguyen et al. (2021) consider that the movement of quasi-liquid and formation of additional hydrates at the neck are governed by the thermodynamics of premelting. Previous studies have shown that the mechanical behavior of the liquid bridge plays an important role in the interaction between hydrate particles.

However, the MMF test results for the gas and liquid phase differ greatly. In early MMF tests, to ensure the stability of the hydrate particle samples, the test was generally carried out in liquid phase solutions such as decane, CP, and water. Subsequently, Aman et al. (2012) tested the cohesion of CP hydrate particles in a normal pressure gas phase environment, and their results revealed that the cohesion value of the hydrate particles in the gas phase was about twice that in the liquid phase. Lee et al. (2014) developed a high-pressure hydrate micromechanical force (HP–MMF) testing device, and they tested the cohesion between hydrate particles formed by methane, carbon dioxide, and a mixture of methane and ethane and the adhesion to the simulated pipe wall (Lee and Sum, 2015). Wang et al. (2020) tested the mechanical behavior of mixed methane and ethane gas hydrate particles in a high-pressure gas phase environment and found that the cohesion was much higher than that of cyclopentane hydrate particles in a liquid phase environment. It was also found that the cohesion of the hydrate particles was independent of the size of the particles in the liquid CP phase, while it was linearly related to the effective radius of the hydrate particles in the gas phase. Liu et al. (2023) carried out a mechanical test on methane hydrate particles and water droplets in a high-pressure gas phase environment and found that as the supercooling degree and contact time increased, the consolidation rate of the liquid bridge increased, and the dominant mechanism of the mechanical behavior was the tensile strength of the hydrate. The differences in the above test results indicate that the mechanical behavior of the liquid bridge may be different in the gas and liquid phase. However, the mechanism of this difference is still unclear. Testing in high-pressure environments is more difficult, however, under high pressure or normal pressure, few MMF tests have been conducted on the mechanical behavior of liquid bridges in a gas phase environment. Therefore, it is necessary to continue to study the mechanical behavior of the liquid bridge in a gas phase environment. The direct mechanical test of hydrate particles and water droplets in a gas phase environment is an effective means of simulating the mechanical behavior of the liquid bridge between hydrate particles.

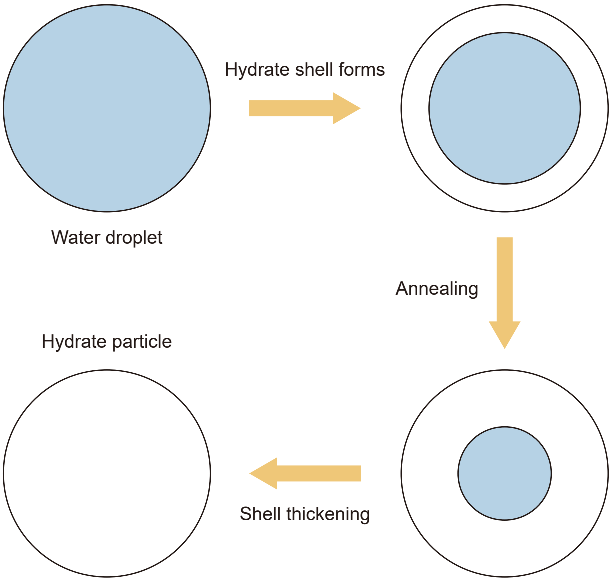

Fig. 1. Water droplets form a hydrate particle model in oil (modified from Taylor et al. (2007)).

In this study, a force sensor with a higher sampling frequency and an electric displacement stage with higher positioning accuracy were used to improve the traditional MMF device for hydrate testing. The mechanical behavior of the liquid bridge during the interaction between THF and CP hydrate particles and water droplets was observed in real time. A possible model was supplemented to explain the observed mechanical behavior of the weakly consolidated liquid bridge. The results of this study contribute to a more comprehensive understanding of the consolidation process of the liquid bridge between hydrate particles in a gas phase environment, and clarify the reasons for the differences in the mechanical behaviors of the liquid bridge between hydrate particles in different phase environments.

2. Experimental study

2.1. Experimental device and testing method

The temperature control system of the improved hydrate MMF test device (Fig. 2) mainly consists of a circulating bath (Julabo ZT4), a temperature control cell, and a temperature sensor (OMEGA SA1-RTD, accuracy of ±0.1 °C). The measuring system consists of three programmable electric displacement stages (PI, positioning accuracy of 0.5 μm and velocity accuracy of 1 μm/s) and two tension-compression force sensors (FUTEK, accuracy of 0.01 mN, sampling frequency of 200 Hz). Tests were carried out in the vertical (N) directions. A microscope equipped with a camera (Olympus SZ61, 65x zoom) was used to record the samples and test movements in the temperature-controlled cell in real time. All of the displacement operations, real-time images, and force curves were processed using dedicated software.

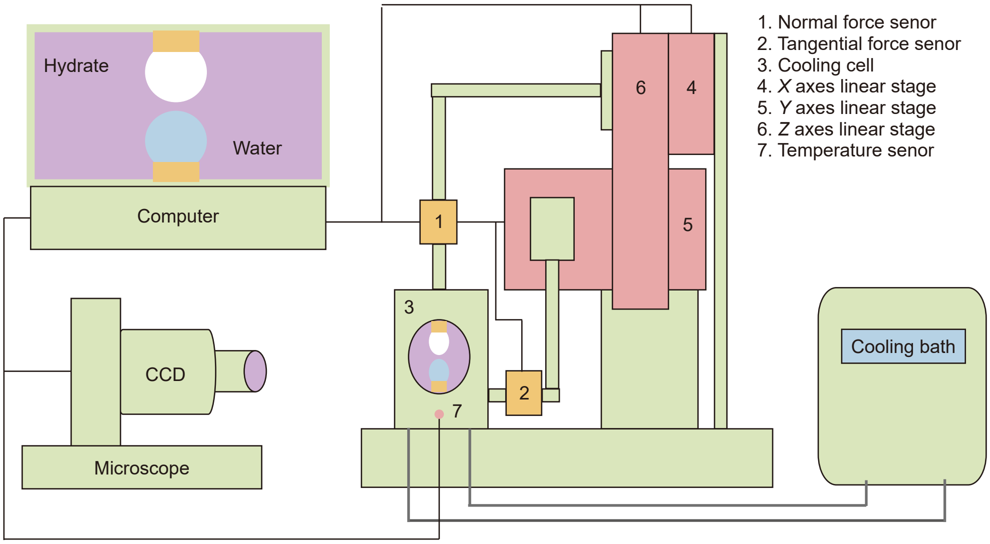

Fig. 2. Improved MMF testing device for hydrates.

2.2. Experimental materials and hydrate formation

THF and CP hydrates can stably exist under atmospheric pressure within 4.4 °C and 7.7 °C, respectively, and their formation method is relatively simple. Therefore, in this study, we used THF and CP (Aladdin Company, purity ≥99.9%) to synthesize hydrates under atmospheric pressure. THF is highly volatile, so the THF hydrate sample was prepared using a THF solution with a mass fraction of 22%, which is slightly higher than the conventional formation concentration of 19% (Peng et al., 2018). The CP hydrates were prepared by soaking ice particles in a CP solution and controlling the temperature (Aman et al., 2013). Deionized water (resistivity 18.25 MΩ·cm) was obtained from a laboratory preparation machine. The details of the hydrate sample formation methods have been described in a previous study (Luo et al., 2022).

2.3. Experimental procedures

The tests of the mechanical behaviors of hydrate particles and water droplets included three steps: contact, pull, and separation (Fig. 3). (1) The electric displacement stage was controlled to adjust the distance between the top particle and the bottom particle (about 20 μm above). After the sensor was zeroed, a step length of 1 μm downward was adopted to achieve contact between the top particle and bottom particle. When contact was made, the force value recorded by the sensor at the moment of contact between the particles and water droplets was called the initial contact force (Song et al., 2010; Liu et al., 2015). (2) After reaching the moment of contact, the liquid bridge narrowed by being pulled upward. In this study, the pull velocity was 1 μm/s and the step size was 1 μm, with a higher accuracy than previous study (10 μm/s). (3) When the liquid bridge was pulled apart, the force recorded by the sensor was defined as the adhesion force. The changes in the force values during the above three steps were recorded by the force sensor in real time (Yu et al., 2021).

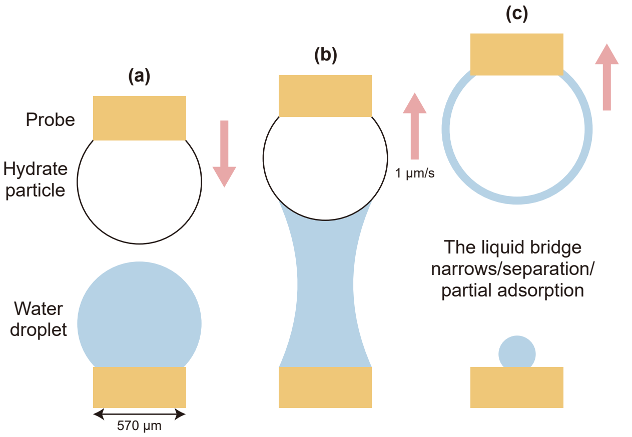

Fig. 3. Method of testing the contact mechanics of the hydrate particles and water droplets **(a)** Contact. **(b)** Pull. **(c)** Separation.

To facilitate comparison with previous studies, some of the measured force values were normalized using the mean harmonic radius R^* of the particles (Eq. (1)). R^* is the mean harmonic radius, and R_1 and R_2 are the radii of the two particles. At least 40 sets of tests were performed on THF, CP hydrate particles, and water droplets, and a new pair of particles was formed in each set of tests. In addition, 60 sets of droplet-to-droplet tests were performed to compare the force curve when the liquid bridge was liquid. It should be noted that to better compare the previous tests conducted in a liquid phase environment, the tests in this study were all carried out in a gas phase environment (air, including volatile gases in the CP and THF solutions, the test temperature was 2 °C, the subcooling degrees for THF and CP hydrates were 2.4 °C and 5.7 °C respectively).

$$R^* = \frac{2R_1R_2}{R_1 + R_2}. \tag{1}$$

3. Results

3.1. Typical liquid bridge morphology and force curve in a gas phase environment

In this study, the typical liquid bridge morphology and force curve in a gas phase environment was divided into unconsolidated, fully consolidated, and weak consolidation morphologies.

(1) The liquid bridge is unconsolidated

When the CP hydrate particles and water droplets were in contact without hydrate growth and consolidation, the liquid bridge was liquid (Fig. 4(a1) P1–P5). In the process of the liquid bridge being pulled apart (Fig. 4(b1) AP1–P5), the initial contact force when the particles came into contact with the liquid bridge (about 0.04 mN, Fig. 4(b1) P2) was close to the adhesion force when the liquid bridge broke (about 0.03 mN, Fig. 4(b1) P4). The force curve of this process was approximately horizontal, which was similar to the test force curve when two water droplets are pulled apart after contacting and merging. Similar horizontal force curves have been found in tests on the contact mechanics between cyclopentane hydrates and water droplets in a liquid phase (Song et al., 2010; Cha et al., 2013; Liu et al., 2015; Liu et al., 2017a). This indicates that the initial contact force between the hydrate particles was close to the adhesion force when the liquid bridge was liquid in the gas and liquid phase.

(2) The liquid bridge is fully consolidated

When the CP hydrate particles were in contact with water droplets and hydrate growth and fully consolidation occurred (Fig. 4(a2) P1–P5), the adhesion of the liquid bridge for tensile breakage was attributed to the tensile strength of the hydrates at the moment of breakage. The force curve (Fig. 4(b2)) exhibited a rapid return to zero after reaching a peak (about 156 mN, Fig. 4(b2) P4). In this example, because the surface adhesion strength of the probe to the hydrates was less than the tensile strength after the consolidation of the liquid bridge, the tensile failure occurred at the upper section of the glass probe (Fig. 4(a2) P5). The adhesion strength between the hydrate particles and the glass section at this time was calculated to be 617 kPa, which is close to the adhesion strength of hydrates on a quartz surface measured in a previous study (about 200 kPa (Jung and Santamarina, 2011)).

(3) Weak consolidation of the liquid bridge

The characteristics and force curve of the liquid bridge in the weak consolidation state were complex. They can be summarized into three categories.

1) Hydrate shells form rapidly on the bridge surface

When the hydrate particles came in contact with the water droplets, a hydrate shell quickly formed on the surface of the liquid bridge, but the hydrate shell was not consolidated with the bottom probe section (Fig. 4(a3) P1–P5). At this time, the force curve (Fig. 4(b3) P1–P5) quickly turned negative (about −0.45 mN, Fig. 4(b3) P3) after the initial contact point (about 0.05 mN, Fig. 4(b3) P2). A similar phenomenon of the direction jump of the force was also found in the work of the predecessors in the liquid phase (Liu et al., 2015; Liu et al., 2016; Liu et al., 2017a). This may be due to the volume expansion of the hydrate shell formation, which compressed the sensor force value. As the liquid bridge was pulled upward, the force curve in the second half (Fig. 4(b3) P3–P5) was similar to that of the liquid bridge described above since the liquid bridge was still liquid.

2) Partial consolidation of the liquid bridge results in a reduced liquid volume

Hydrate growth occurred on the top of the hydrate particles at the liquid-solid interface of the liquid bridge, which resulted in

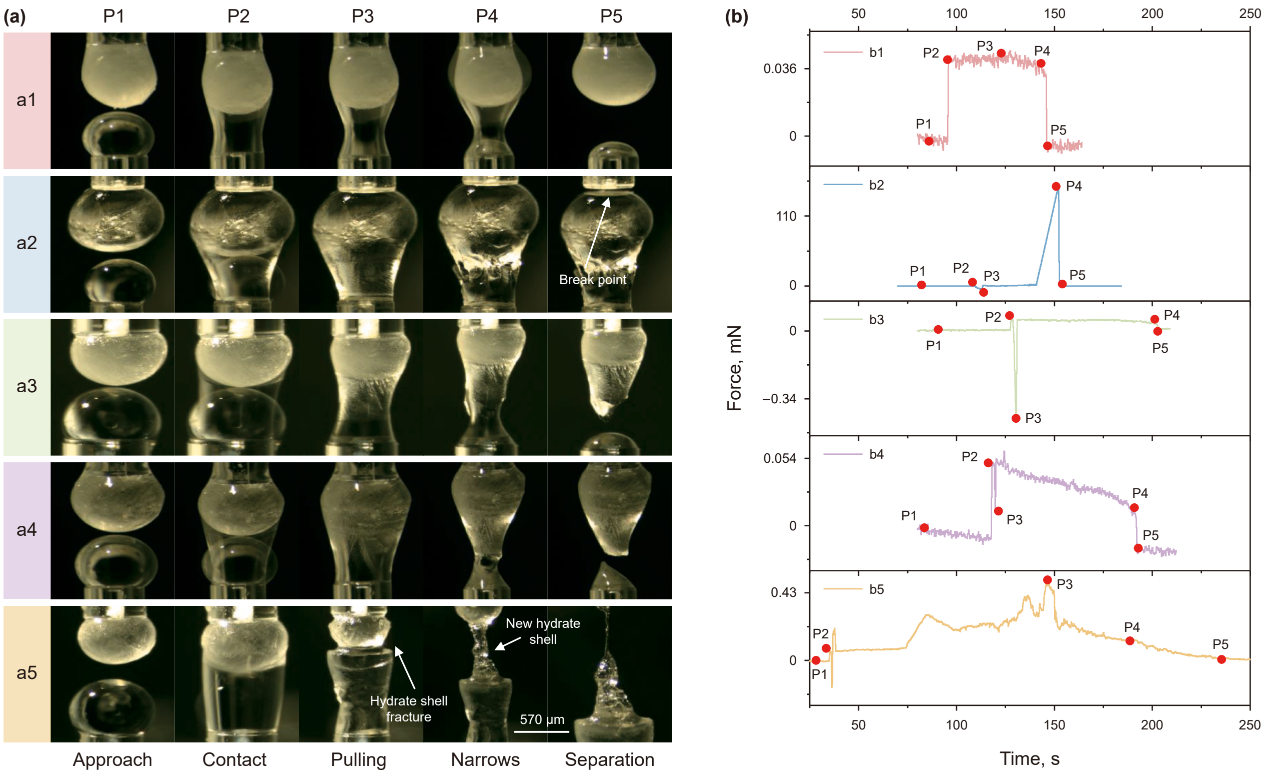

Fig. 4. Typical morphology **(a)** and real time force curves **(b)** of a hydrate particle-water droplet liquid bridge in a gas phase environment: (a1) Unconsolidated; (a2) Fully consolidated; (a3–a5) Weak consolidation; (a3) Hydrates form on part of the surface; (a4) Partial consolidation results in a reduced liquid volume; (a5) New hydrate shell forms at the fracture.

decreases in the volume of the liquid and the breaking force of the liquid bridge (Fig. 4(a4)). At this time, the force curve inclined to the right (Fig. 4(b4)). The initial contact force was about 0.05 mN (Fig. 4(b4) P2) but the adhesion force was about 0.01 mN (Fig. 4(b4) P4). Similar force curves have been obtained in previous tests on the breakage of the contact between CP hydrates and water droplets in a liquid phase environment (Liu et al., 2017a; Liu et al., 2020).

3) New hydrate shell forms at the fracture

In a gas phase environment, the hydrate shell on the surface of the liquid bridge was pulled off, and the unconverted water inside forms a new hydrate shell at the fracture. This process was repeated until the liquid bridge was stretched into a long thin filament and then breaks. At this time, the length of the stretched liquid bridge can reach several times the diameter of the particle (Fig. 4(a5) P1–P5). The process force curve contained multiple continuous peaks and slowly returned to zero (Fig. 4(b5) P1–P5). At this time, the force value when the liquid bridge was broken (Fig. 4(b5) P5) was not the maximum force value (about 0.50 mN, Fig. 4(b5) P3) in the process of breaking the liquid bridge. This is different from the previous observation results. In previous studies, the force value at the time of liquid bridge rupture was the maximum and was defined as the adhesion force.

3.2. *Characteristics of liquid bridge consolidation in a gas phase environment*

(1) Observations of hydrate growth in a liquid bridge

In the gas phase test, after the hydrate particles with different compositions of THF and CP were in contact with the water droplets, the rapid growth of hydrates was observed in the liquid bridge (Fig. 5(a1–a4)). After the hydrate particles were in contact with the water droplets (Fig. 5(a1)), the water droplets quickly diffuse on the surface of the hydrate particles (Fig. 5(a2)), and the hydrate-water-gas three phase contact (TPC, Fig. 5(a3))line immediately formed and expanded on the surface of the hydrate particles (Liu et al., 2020). The hydrates grew along the gas–liquid surface of the liquid bridge, and the contour of the hydrate shell almost coincided with the contour of the liquid bridge. Hydrate grows from the solid-liquid interface and gas-liquid surface to the inside of the liquid bridge, and finally fully consolidated (Fig. 5(a4)). The same hydrate growth phenomenon has been observed in a liquid phase environment (Cha et al., 2013; Liu et al., 2015; Liu et al., 2016; Liu et al., 2017a; Liu et al., 2020), indicating that the growth process of the hydrates in the liquid bridge was similar in the gas and liquid phase. This growth process conforms to the shell formation theory of hydrate particles formed by water droplets in oil and gas pipelines proposed by Taylor et al. (2007). The results of liquid phase environment show that hydrate particles act as seeds, and high supercooling generates high nucleation driving force, leading to hydrate growth on the liquid bridge (Liu et al., 2015, 2016). In this study, this may have been caused by the poor gas-hydraulic pressure and the dispersion of the THF and CP gases in the gas phase environment, which provided part conditions for the growth of hydrate particle seeds on the liquid bridge.

The above process also produced obvious changes in the real-time curve of the force (Fig. 5(b1–b4)). At the contact point, due to the reason that the interfacial Gibbs free energy would be reduced to a relatively lower value towards an equilibrium state (Liu et al., 2015), water droplets wet the surface of the hydrate particles, a downward pull was generated on the probe, and the force curve exhibited a positive peak (about 0.06 mN, Fig. 5(b2)). Subsequently, may be due to the rapid formation of hydrate shells on the surface of the liquid bridge, the probe was compressed upward, and the force curve quickly transformed into a large negative peak (about −0.67 mN, Fig. 5(b3)). As the hydrate began to grow into the unconverted water, a dynamic process of growth and consolidation occurred inside the liquid bridge. This may have been due to the difference in the guest concentration between the water droplets and the hydrate particles. In this process, the real-time force curve changed continuously in the direction of the force value until the liquid bridge was completely consolidated and the force value became stable at zero (Fig. 5(b4)). The hydrate growth velocity was calculated by the height of the liquid bridge (measured by Image J) and the time from the contact point to the stabilization of the force curve. Under the gas phase condition, the

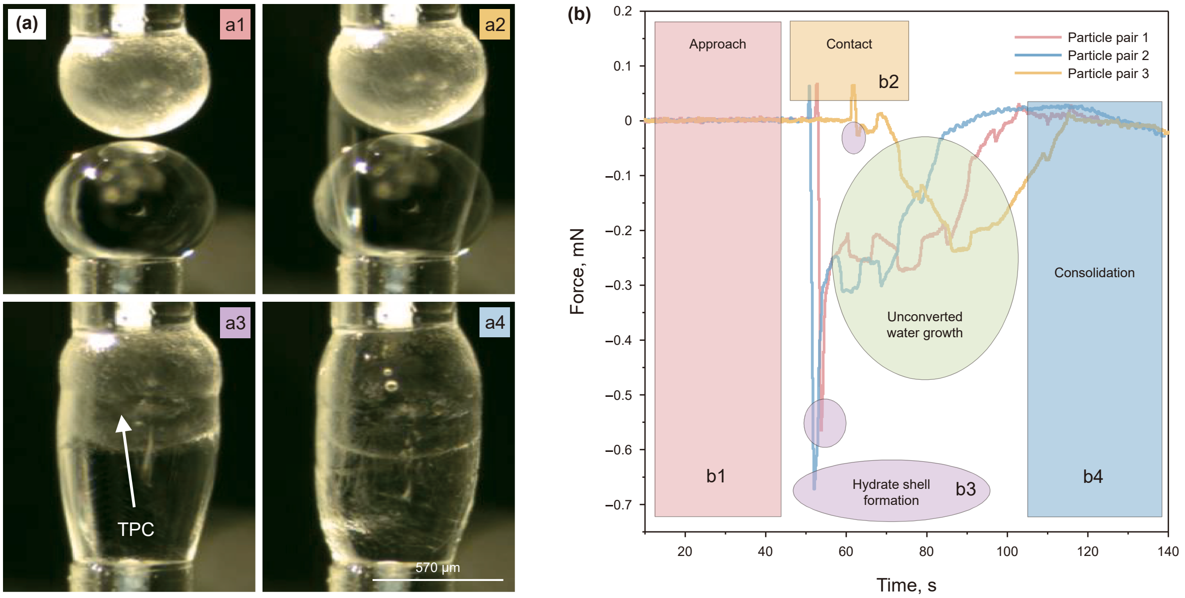

Fig. 5. Real time image **(a)** and force curve **(b)** of the growth of the THF hydrate particles in contact with the water droplets in a gas phase environment.

hydrate growth velocity of the THF and CP hydrate particles in contact with the water droplets were approximately 5–9 and 14–17 μm/s respectively (the subcooling degrees were 2.4 °C and 5.7 °C respectively). These values are greater than the growth velocity of cyclopentane hydrates observed in the liquid phase (about 1.5 μm/s (Liu et al., 2020) and 6 μm/s (Brown and Koh, 2016), the subcooling degrees were 4.7 °C and 7.4 °C respectively).

(2) Compression test during growth of the liquid bridge

To further clarify the growth characteristics of the hydrates on the liquid bridge in a gas phase environment, compression tests were conducted during the growth of THF hydrate particles in contact with water droplets (Fig. 6(a1–a4)). After the hydrate particles made contact with the water droplets (Fig. 6(a2)), the hydrates began to grow on the gas-liquid surface (Fig. 6(a3)). At this time, the compression continued downward at a speed of 1 μm/s, and the unconverted water inside the liquid bridge was squeezed and wrapped around the surface of the hydrate particles. After about 20 s, the hydrate particles and liquid bridge were compressed from a cylinder into an ellipsoid and were finally consolidated (Fig. 6(a4)).

As can be seen from the real-time curve of the force during compression (Fig. 6(b1–b4)), at the time of contact, the sensor recorded a positive value (about 0.05 mN, Fig. 6(b2)). As the hydrate shell grew, the force value rapidly became negative (about −0.46 mN, Fig. 6(b3)), it continued to compress downward, the force value changed to positive, and it remained near zero under compression. Until the hydrates consolidated, the force value changed from nearly zero to a large negative value (about −1.04 mN, and then, it rebounded slightly (Fig. 6(b4)).

This indicates that in the initial growth stage of the liquid bridge, the hydrate shell could only withstand small loads, and it completely lost its bearing capacity after being compressed into the unconverted water. With the gradual consolidation of the unconverted water, the hydrate shell began to resist larger loads. This verifies the hydrate growth characteristics discussed above based on the force curve. According to the preliminary calculations of the ratio of the peak load value to the height of the liquid bridge under compression, the result is 714–3414 mN/m, which is larger than the value for a capillary glass fiber piercing the hydrate shell reported in a previous study (200 mN/m, 0 °C, 90 s, the diameter of the glass fiber is 35 μm (Brown and Koh, 2016)). This may be mainly due to the difference in the thickness of the hydrate shell caused by the different hydrate growth rates and growth times in the gas phase environment.

3.3. *Effects of hydrate particle properties on the mechanics of the unconsolidated liquid bridge*

In this study, we conducted tests in a normal pressure gas phase environment, and it was found that the initial contact force between the particles and water droplets (about 0.20 mN) was proportional to the particle diameter (100–500 μm) of the particles and droplets (Fig. 7(a)–(c)). Similar conclusions can be found in previous work, that the adhesion is linearly related to the effective radius of the particle and the volume of the water droplet (Cha et al., 2013; Wang et al., 2020) (Fig. 7(c)). Through effective radius treatment of the particle size (Fig. 7(d)), it was found that the initial contact force between the CP hydrate particles and water droplets is about 120 mN/m in this study, which is about 50 mN/m in previous tests under liquid phase conditions. This is similar to the conclusion that the test value of the adhesion between hydrate particles in the gas phase is about twice that in the oil phase (Aman et al., 2012).

In addition, it has been found that the initial contact force between sand particle and water droplets is the largest (about 200 mN/m) in the gas phase (Fig. 7(d)). Possible reasons for the above differences are 1) different interfacial tension and pressure. The interfacial tension and the internal and external pressure differences of the liquid bridge are proportional to the interparticle force (Aman et al., 2011; Liu et al., 2020). In the gas phase, the surface tension between water and air is about 75 mN/m, which is larger than the oil–water interfacial tension in the liquid phase. The interfacial tension between water and decane is 52 mN/m (Zeppieri et al., 2001), and the interfacial tension between water and cyclopentane is 42 mN/m (Lin et al., 2010). Moreover, these pressure differential effects are weaker in the liquid phase environment. 2) Particle surface roughness: As the surface of a hydrate particle is rougher than that in the liquid phase (Wang et al., 2020),

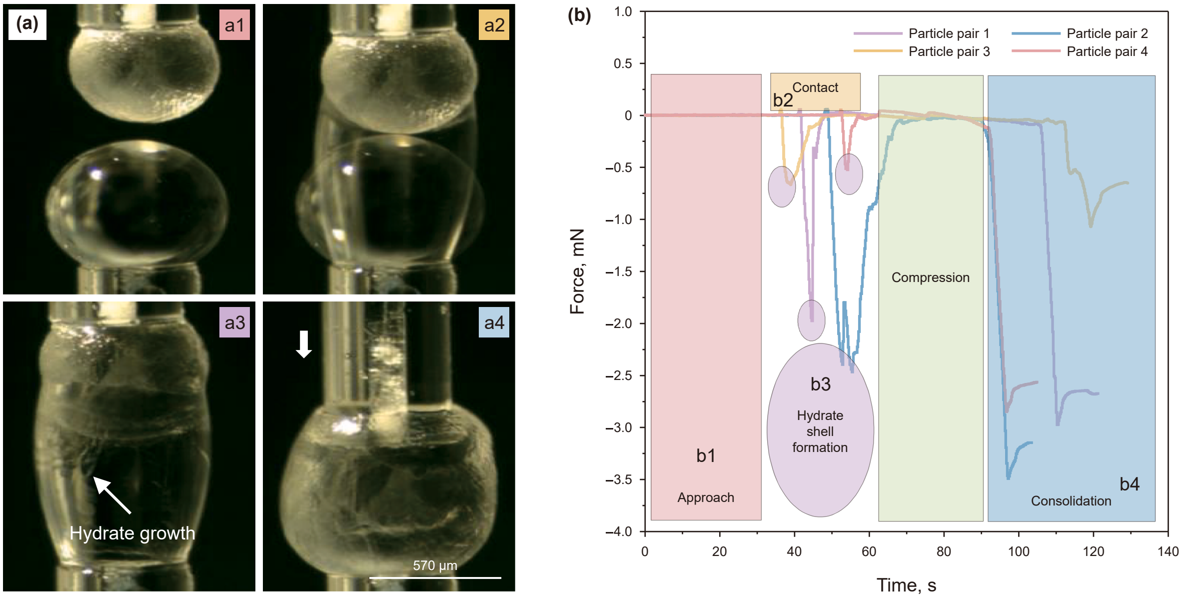

Fig. 6. Real time image **(a)** and force curve **(b)** for the compression test during the growth of THF hydrate particles in contact with water droplets in a gas phase environment.

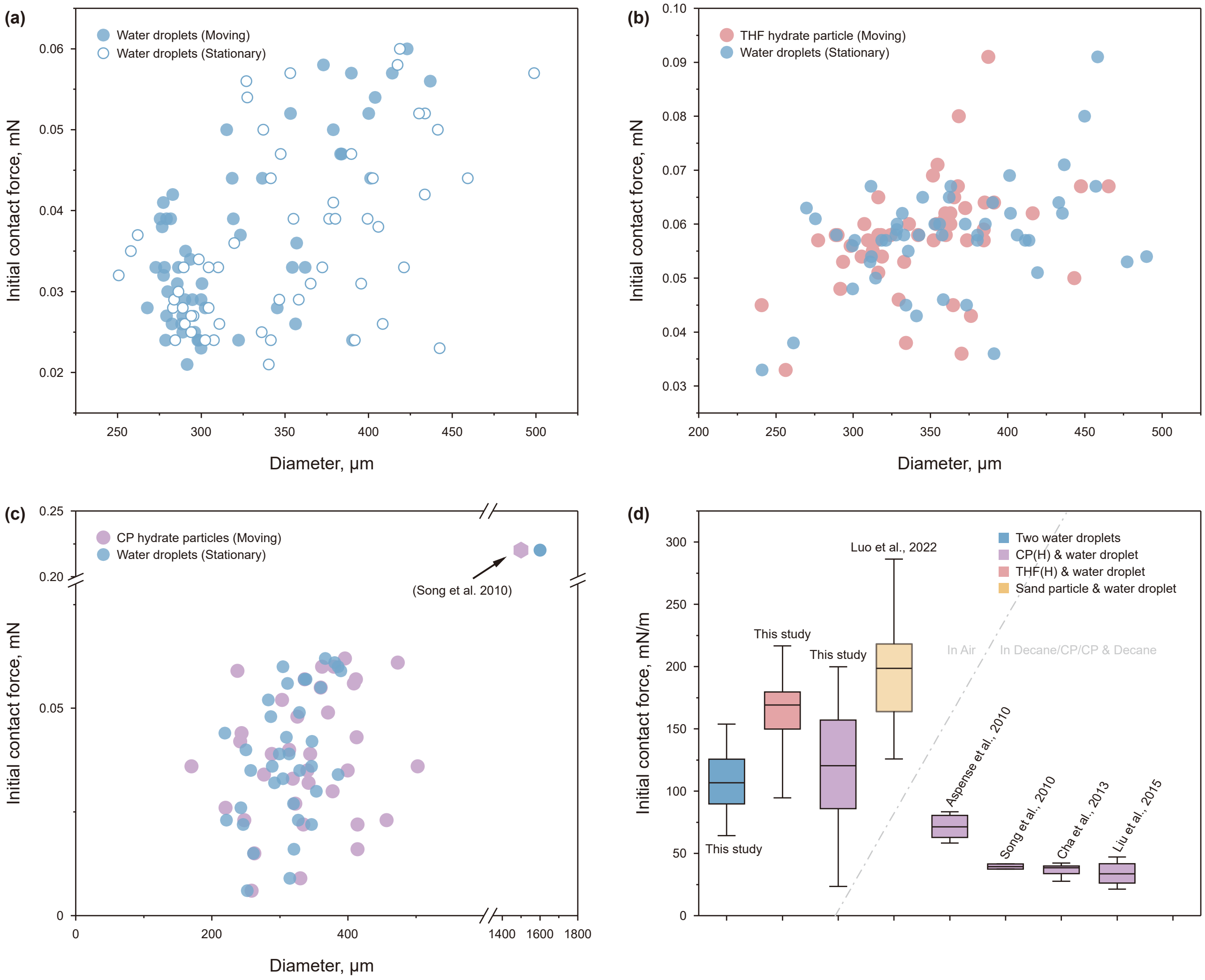

Fig. 7. Comparison of initial contact force values. **(a)** Two water droplets. **(b)** THF hydrate and water droplets. **(c)** CP hydrate and water droplets. **(d)** Comparison of results after normalized radius treatment.

hydrate particles in the gas phase have a larger surface area and greater interfacial energy, which can be further explained through comparison of sand particle. As a result, the test values of the adhesion between hydrate particles are different in the gas and liquid phase environments when the liquid bridge is unconsolidated.

4. Discussion

4.1. Mechanical calculation model of a liquid bridge in the weak consolidation state

In the above three typical states of weak consolidation of liquid bridges, when hydrate shells are rapidly formed on the surface of a liquid bridge (Fig. 4(a3)), the liquid bridge is similar to the state of unconsolidated liquid bridges (Fig. 4(a1)). In this case, the mechanical behavior between hydrate particles and water droplets is dominated by the capillary liquid bridge force, and the interparticle force can be calculated using Aman et al.'s model. The model considers both capillary bridge theory and hydrate consolidation. When the liquid bridge is fully consolidated (Fig. 4(a2) in this study), the inter-particle mechanics calculation is determined by the tensile strength of the hydrates and the consolidation area of the liquid bridge. However, Aman et al.'s model is not applicable to the case of liquid volume reduction caused by partial consolidation of the liquid bridge (Fig. 4(a4) in this study). For this case, Liu et al. (2020) established a modified hydrate interparticle mechanics calculation model based on Aman et al.'s model and the hydrate shell formation theory. This model considers the partial consolidation of the capillary liquid bridge in the calculation and simulation of the interaction between hydrate particles and water droplets when the liquid volume decreases during hydrate growth on a liquid bridge (Liu et al., 2016; Liu et al., 2017b; Liu et al., 2020).

Among the above existing models, Aman et al.'s model does not consider the state of weak consolidation of the liquid bridge, and it lacks a description of the consolidation characteristics of the liquid bridge, resulting in a small correspondence between the calculated value of the model and the measured force curve when the model is fully consolidated. A comparison of the model calculation results is presented in Fig. 9(a). In addition, Liu et al.'s model only takes into account the reduction of the amount of weakly consolidated liquid in the liquid bridge, and it does not take into account the special weak consolidation state of the hydrate shell regenerated at the pull break of the liquid bridge observed in this study (Fig. 4(a5)). In view of the above shortcomings, based on the above model and the hydrate shell formation model, we supplemented a

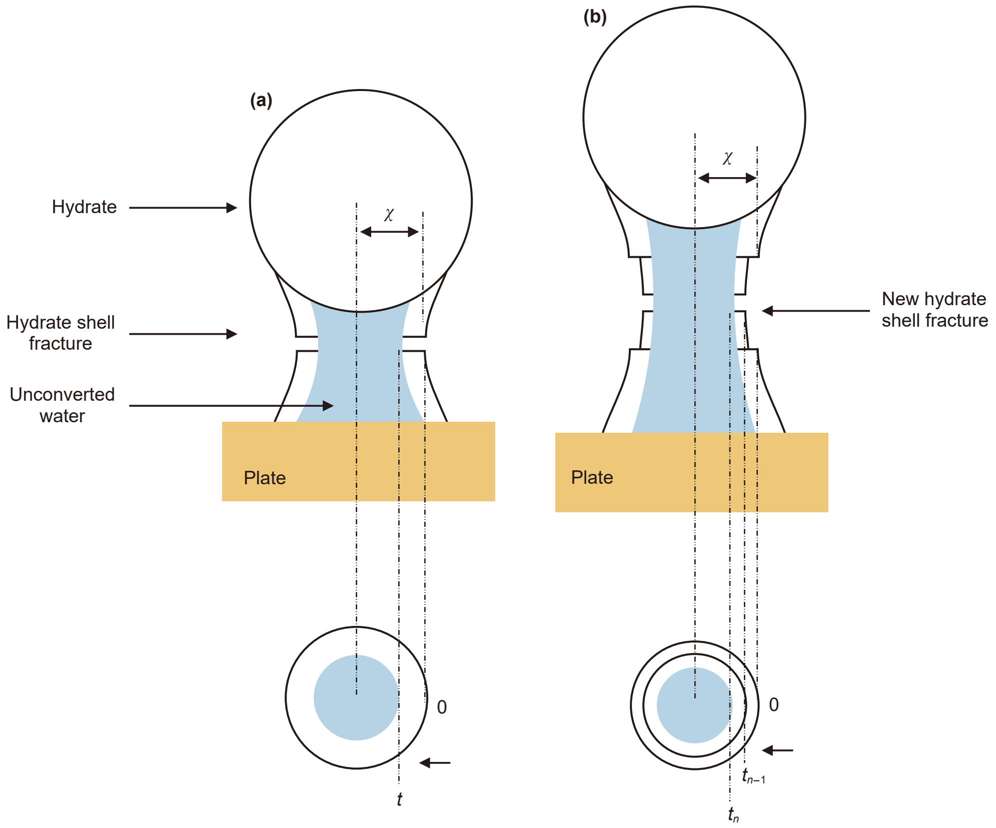

Fig. 8. Simplified calculation model for weak consolidation of hydrate particles in a gas phase environment. **(a)** Model 1: No new hydrate shell is formed at the fracture, **(b)** Model 2: New hydrate shell forms at the fracture.

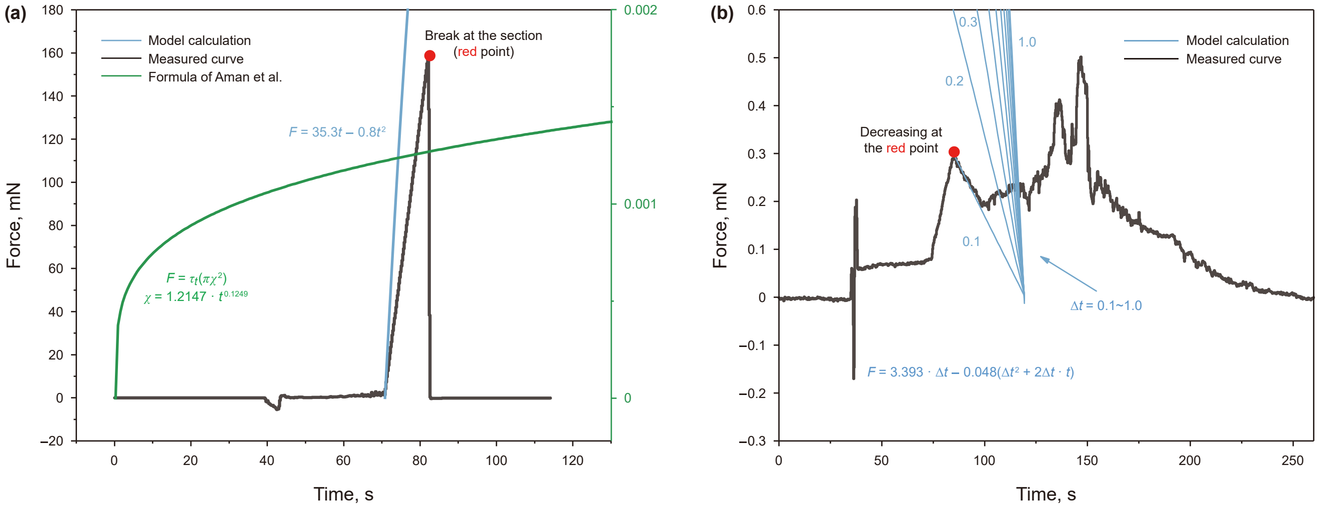

Fig. 9. Comparison between the calculated results of the two models and the measured curves **(a)** No new hydrate shell is formed at the CP hydrate fracture; **(b)** New hydrate shell is formed at the THF hydrate fracture.

possible liquid bridge weak consolidation model for a gas phase environment (Fig. 8).

(1) Model 1: No new hydrate shell is formed at the fracture

In this case, the tensile force of the weakly consolidated liquid bridge is attributed to the strength of the hydrate shell ring, and when the liquid bridge is fully consolidated, the tensile force is equal to the tensile strength of the entire hydrate cylinder (Fig. 8(a)). This model refers to Aman et al.'s model to better describe the characteristics of the hydrate growth from the surface of the liquid bridge to the interior in the gas phase environment. The model assumes that the expansion of the hydrates in the growth and consolidation process is negligible relative to the diameter of the liquid bridge, and the value of the liquid bridge force in the unconverted water is ignored. The hydrate shell is

Table 1
List of calculation parameters.

Classes	Model 1	Model 2
τ_t	0.91 MPa (CP hydrate is a type II hydrate (Aman et al., 2011), Literature reference value)	0.17 MPa (THF hydrate (Jung and Santamarina, 2011), Literature reference value)
V	17 μm/s (Measured in this study)	9 μm/s (Measured in this study)
χ	363 μm (Measured in this study)	316 μm (Measured in this study)
Equation	$F = 35.3 \cdot t - 0.8 \cdot t^2$ (The parameters were substituted to the equation)	$F = 3.393 \cdot \Delta t - 0.048(\Delta t^2 + 2\Delta t \cdot t)$ (The parameters were substituted to the equation)
Remarks	The interval Δt between two hydrate shells that have been pulled off cannot be determined. In Fig. 9(b), 1.0–0.1 was taken, where $\Delta t = 0.1$ corresponds better to the measured force curve.	

eventually consolidated into the entire cylinder by the ring, and the ring area of the hydrate shell at a certain time is

$$S = \pi\chi^2 - \pi(\chi - Vt)^2 = 2\pi\chi Vt - \pi(Vt)^2 \tag{7}$$

The breaking force at this time is

$$F = \tau_t \left[2\pi\chi Vt - \pi(Vt)^2\right], t \le \frac{\chi}{V} \tag{8}$$

where τ_t is the tensile strength of the hydrate, χ is the radius of the liquid bridge in the contact area, t is the contact time, and V is the growth rate of the hydrate under the gas phase condition.

(2) Model 2: New hydrate shells forms at the fracture

After the liquid bridge hydrate shell is pulled apart, the unconverted water inside the liquid bridge forms a new hydrate shell during the pull-off process (Fig. 8(b)). In this model, due to the uncertainty of the interval time Δt between the pulling off of two hydrate shells, the thickness of the hydrate shell rings will be inconsistent, and the force curve will have multiple peaks when the hydrate shell breaks.

In this case, the change in the area of the hydrate shell ring with time can be expressed as follows:

$$\begin{aligned} S = S_{t_n} - S_{t_{n-1}} &= \left[2\pi\chi V t_n - \pi(Vt_n)^2\right] - \left[2\pi\chi V t_{n-1} - \pi(Vt_{n-1})^2\right] \\ &= 2\pi\chi V(t_n - t_{n-1}) - \pi V^2\left(t_n{}^2 - t_{n-1}^2\right) \end{aligned} \tag{9}$$

At this time, the breaking force is

$$F = \tau_t \left[2\pi\chi V(t_n - t_{n-1}) - \pi V^2\left(t_n{}^2 - t_{n-1}^2\right)\right], t \le \frac{\chi}{V} \tag{10}$$

where $t_n - t_{n-1} = \Delta t$ is the time between the pulling off of two successive hydrate shells. At this time,

$$F = \tau_t \left[2\pi\chi V(\Delta t) - \pi V^2\left(\Delta t^2 + 2\Delta t \cdot t_{n-1}\right)\right], t \le \frac{\chi}{V} \tag{11}$$

4.2. Comparison of the calculated results of the model and the measured force curve

By comparing the model calculation results with the measured force curve, it was found that the model calculation results are close to the experimental results over time. Model 1 is quite consistent with the force curve characteristic that no new hydrate shell is formed at the CP hydrate fracture (Fig. 9(a)). The tensile force increases rapidly, and the force curve rapidly slopes upward to zero at the maximum peak value (Time and force was about 75 s and 156 mN respectively). Compared with the previous models, the calculated results of our model are closer to the measured force curve. Model 2 explains the force curve characteristic of the formation of a new hydrate shell at the THF hydrate fracture (Fig. 9(b)). The force curve contains multiple peaks, and it decreases at a peak, but it does not return to zero. In this example, where $\Delta t = 0.1$ and the force value is about 0.28 mN at 84 s, the calculated force value curve starts to decrease, which is close to the measured curve. During the calculation of the model, τ_t is the previous test results, and χ is the radius of the liquid bridge in the contact area (obtained from the measured of Image J). The calculation parameters are described in Table 1.

5. Conclusions

Previous MMF tests between hydrate particles have shown that the adhesion force values vary significantly between the gas and liquid phase environment. However, due to the relatively insufficient testing work conducted in the gas environment, the mechanism behind these differences is still unclear. In this study, the typical morphology and consolidation characteristics of a liquid bridge during the contact and pull-off processes between hydrate particles and water droplets were observed using an improved hydrate MMF testing device in a gas phase environment. The influences of the particle properties on the capillary liquid bridge force were investigated. A simplified calculation model that considers the weak consolidation state of the liquid bridge was established. The reasons for the differences between the gas and liquid phase in the MMF test of hydrates were discussed and analyzed. The findings of this study are summarized below.

(1) Under the gas phase condition, when the particle size is 100–500 μm, the initial contact force between hydrate particles and water droplets is about 0.20 mN. When a hydrate shell is formed on the surface of the liquid bridge, the sensor will feel the extrusion pressure value of 0.46–2.36 mN. When the liquid bridge is fully consolidated, the force value of pulling the hydrate from the section of the probe can reach 156 mN. This shows that the consolidation process of hydrate plays a decisive role in the change of the mechanical property of the liquid bridge.

(2) When hydrate particles are in contact with water droplets in the gas phase, hydrate shells easily form on the surface of the liquid bridge. The hydrate growth velocity of the THF and CP hydrate particles in contact with the water droplets were approximately 5–9 and 14–17 μm/s respectively. And the initial contact force between the CP hydrate particles and water droplets is about 120 mN/m. Which are higher than those for the liquid phase reported in previous studies.

(3) The interfacial tension, pressure difference, and surface roughness of hydrate particles are greater in the gas phase than in the liquid phase. This may be the main reason for the difference between the test results for hydrate particles in

different test environments when the liquid bridge is unconsolidated.

(4) Under the gas phase condition, the liquid bridge will exhibit a more obvious weak consolidation phenomenon, and complex mechanical behavior will occur during the tensile fracturing of the liquid bridge. Multiple peaks will appear in the corresponding force curve, which causes the measured force values for gas and liquid phase environments to exhibit more differences and instability.

(5) A simplified calculation model for the weak consolidation of a liquid bridge in a gas phase environment was supplemented to explain the observed weak consolidation of the liquid bridge, on which hydrate shells continuously form and are pulled off. A comparison with the measured force curve preliminarily verifies this model.

However, this model cannot explain the exponential decline of the force curve at the end of the real-time force curve for a weakly consolidated liquid bridge (Fig. 4(a5)), which exhibits creep characteristics (Fig. 4(b5) P4–P5). During the process of the hydrate shell being broken, the failure of the shell's extensibility, the expansion of cracks, and the viscoelastic effect of the consolidated structure are all possible causes for the aforementioned changes in the force curve. In the subsequent research, we will attempt to characterize the above speculation and analyze the relationship between the creep characteristics and the viscosity of the internal unconverted water.

CRediT authorship contribution statement

Qiang Luo: Writing – review & editing, Writing – original draft, Investigation, Formal analysis, Data curation, Conceptualization. **Zhi-Hui Liu:** Validation, Formal analysis. **Xiao-Feng Dou:** Methodology, Formal analysis. **De-Li Gao:** Supervision. **Zhi-Chao Liu:** Writing – review & editing, Supervision, Project administration, Funding acquisition. **Fu-Long Ning:** Writing – review & editing, Supervision, Project administration, Funding acquisition, Conceptualization.

Declaration of interests

The authors declare that they have no known competing financial interests or personal relationships that could have appeared to influence the work reported in this paper.

Acknowledgements

This research was supported by the National Natural Science Foundation of China (42225207, 42376220, 42506225), the Science and Technology Projects in Key Areas of Nansha District (2023ZD017), the Guangdong Basic and Applied Basic Research Foundation (2020B0301030003), Open Fund of the Innovation Base of Fine Mine Prospecting and Intelligent Monitoring Technology (Grant No. 2024-MPIM-03), the Engineering Research Center of Rock-Soil Drilling & Excavation and Protection Open Fund (Grant No. 202504). We thank LetPub (www.letpub.com) for its linguistic assistance during the preparation of this manuscript.

References

Aman, Z.M., Koh, C.A., 2016. Interfacial phenomena in gas hydrate systems. Chem. Soc. Rev. 45, 1678–1690. https://doi.org/10.1039/c5cs00791g.

Aman, Z.M., Dieker, L.E., Aspenes, G., et al., 2010. Influence of model oil with surfactants and amphiphilic polymers on cyclopentane hydrate adhesion forces. Energy Fuel. 24, 5441–5445. https://doi.org/10.1021/ef100762r.

Aman, Z.M., Brown, E.P., Sloan, E.D., et al., 2011. Interfacial mechanisms governing cyclopentane clathrate hydrate adhesion/cohesion. Phys. Chem. Chem. Phys. 13, 19796–19806. https://doi.org/10.1039/c1cp21907c.

Aman, Z.M., Joshi, S.E., Sloan, E.D., et al., 2012a2012. Micromechanical cohesion force measurements to determine cyclopentane hydrate interfacial properties. J. Colloid Interface Sci. 376, 283–288. https://doi.org/10.1016/j.jcis.2012.03.019.

Aman, Z.M., Sloan, E.D., Sum, A.K., et al., 2012b2012. Lowering of clathrate hydrate cohesive forces by surface active carboxylic acids. Energy Fuel. 26, 5102–5108. https://doi.org/10.1021/ef300707u.

Aman, Z.M., Olcott, K., Pfeiffer, K., et al., 2013. Surfactant adsorption and interfacial tension investigations on cyclopentane hydrate. Langmuir 29, 2676–2682. https://doi.org/10.1021/la3048714.

Aman, Z.M., Sloan, E.D., Sum, A.K., et al., 2014. Adhesion force interactions between cyclopentane hydrate and physically and chemically modified surfaces. Phys. Chem. Chem. Phys. 16, 25121–25128. https://doi.org/10.1039/c4cp02927e.

Aspenes, G., Dieker, L.E., Aman, Z.M., et al., 2010. Adhesion force between cyclopentane hydrates and solid surface materials. J. Colloid Interface Sci. 343, 529–536. https://doi.org/10.1016/j.jcis.2009.11.071.

Brown, E.P., Koh, C.A., 2016. Micromechanical measurements of the effect of surfactants on cyclopentane hydrate shell properties. Phys. Chem. Chem. Phys. 18, 594–600. https://doi.org/10.1039/c5cp06071k.

Cha, M., Couzis, A., Lee, J.W., 2013. Macroscopic investigation of water volume effects on interfacial dynamic behaviors between clathrate hydrate and water. Langmuir 29, 5793–5800. https://doi.org/10.1021/la4005664.

Collett, T., Bahk, J.-J., Baker, R., et al., 2014. Methane hydrates in nature—current knowledge and challenges. J. Chem. Eng. Data 60, 319–329. https://doi.org/10.1021/je500604h.

Delgado-Linares, J.G., Majid, A.A.A., Sloan, E.D., et al., 2013. Model water-in-oil emulsions for gas hydrate studies in oil continuous systems. Energy Fuel. 27, 4564–4573. https://doi.org/10.1021/ef4004768.

Dieker, L.E., Aman, Z.M., George, N.C., et al., 2009. Micromechanical adhesion force measurements between hydrate particles in hydrocarbon oils and their modifications. Energy Fuel. 23, 5966–5971. https://doi.org/10.1021/ef9006615.

Hu, S.J., Koh, C.A., 2017. Interfacial properties and mechanisms dominating gas hydrate cohesion and adhesion in liquid and vapor hydrocarbon phases. Langmuir 33, 11299–11309. https://doi.org/10.1021/acs.langmuir.7b02676.

Jung, J.W., Santamarina, J.C., 2011. Hydrate adhesive and tensile strengths. G-cubed 12, 1–9. https://doi.org/10.1029/2010gc003495.

Koh, C.A., Sloan, E.D., Sum, A.K., et al., 2011. Fundamentals and applications of gas hydrates. Annu. Rev. Chem. Biomol. Eng. 2, 237–257. https://doi.org/10.1146/annurev-chembioeng-061010-114152.

Lee, B.R., Sum, A.K., 2015. Micromechanical cohesion force between gas hydrate particles measured under high pressure and low temperature conditions. Langmuir 31, 3884–3888. https://doi.org/10.1021/acs.langmuir.5b00361.

Lee, B.R., Koh, C.A., Sum, A.K., 2014. Development of a high pressure micromechanical force apparatus. Rev. Sci. Instrum. 85, 95120–95124. https://doi.org/10.1063/1.4896661.

Lin, S.Y., Mckeigue, K., Maldarelli, C., 2010. Diffusion-controlled surfactant adsorption studied by pendant drop digitization. Aiche Journal 36, 1785–1795.

Liu, C.W., Li, M.Z., Zhang, G.D., et al., 2015. Direct measurements of the interactions between clathrate hydrate particles and water droplets. Phys. Chem. Chem. Phys. 17, 20021–20029. https://doi.org/10.1039/c5cp02247a.

Liu, C.W., Li, M.Z., Liu, C.T., et al., 2016. Micromechanical interactions between clathrate hydrate particles and water droplets: Experiment and modeling. Energy Fuel. 30, 6240–6248. https://doi.org/10.1021/acs.energyfuels.6b00668.

Liu, C.W., Li, M.Z., Chen, L.T., et al., 2017a. Experimental investigation on the interaction forces between clathrate hydrate particles in the presence of a water bridge. Energy Fuel. 31, 4981–4988. https://doi.org/10.1021/acs.energyfuels.7b00364.

Liu, C.W., Li, Y.X., Wang, W.Y., et al., 2017b. Modeling the micromechanical interactions between clathrate hydrate particles and water droplets with reducing liquid volume. Chem. Eng. Sci. 163, 44–55. https://doi.org/10.1016/j.ces.2017.01.031.

Liu, C.W., Zhang, C.R., Zhou, C.R., et al., 2020. Effects of the solidification of capillary bridges on the interaction forces between hydrate particles. Energy Fuel. 34, 4525–4533. https://doi.org/10.1021/acs.energyfuels.0c00463.

Liu, C.W., Zhou, C.R., Li, M.Z., et al., 2023. Direct measurements of the interactions between methane hydrate particle-particle/droplet in high pressure gas phase. Fuel 332, 12619001. https://doi.org/10.1016/j.fuel.2022.126190.

Luo, Q., Liu, Z.H., Ning, F.L., et al., 2022. Micromechanical tangential force measurements between tetrahydrofuran hydrate particles. Fuel 316, 12307301–12307308. https://doi.org/10.1016/j.fuel.2021.123073.

Luo, Q., Li, W., Liu, Z.-H., et al., 2024. Research progress on micro-force measurement of a hydrate particle system. Pet. Sci. 21, 2169–2183. https://doi.org/10.1016/j.petsci.2024.03.017.

Nguyen, N.N., Berger, R., Butt, H.-J., 2020. Premelting-induced agglomeration of hydrates: theoretical analysis and modeling. ACS Appl. Mater. Interfaces 12, 14599–14606. https://doi.org/10.1021/acsami.0c00636.

Nguyen, N.N., Berger, R., Kappl, M., et al., 2021. Clathrate adhesion induced by quasi-liquid layer. J. Phys. Chem. C Nanomater Interf. 125, 21293–21300. https://doi.org/10.1021/acs.jpcc.1c06997.

Nicholas, J.W., Dieker, L.E., Sloan, E.D., et al., 2009. Assessing the feasibility of hydrate deposition on pipeline walls–adhesion force measurements of clathrate hydrate particles on carbon steel. J. Colloid Interface Sci. 331, 322–328. https://doi.org/10.1016/j.jcis.2008.11.070.

Peng, L., Ning, F.L., Li, W., et al., 2018. Investigation on the effect of growth temperature and contact interface on surface characteristics of THF clathrate hydrates by atomic force microscopy. SCI. SINICA Phys. Mech. Astronom. 49 (3), 034612. https://doi.org/10.1360/sspma2018-00182.

Sato, J., Iida, T., Kiyono, F., et al., 2016. Cohesion force measurement of methane hydrate and numerical simulation of rising bubbles covered with a hydrate membrane within a contracting pipe. Energy Fuel. 30, 7100–7107. https://doi.org/10.1021/acs.energyfuels.6b01341.

Sloan Jr., E.D., 2003. Fundamental principles and applications of natural gas hydrates. Nature 426, 353–359. https://doi.org/10.1038/nature02135.

Sloan, E.D., 2004. Introductory overview: Hydrate knowledge development. Am. Mineral. 89, 1155–1161. https://doi.org/10.2138/am-2004-8-901.

Song, J.H., Couzis, A., Lee, J.W., 2010a2010. Direct measurements of contact force between clathrate hydrates and water. Langmuir 26, 9187–9190. https://doi.org/10.1021/la101309j.

Song, J.H., Couzis, A., Lee, J.W., 2010b2010. Investigation of macroscopic interfacial dynamics between clathrate hydrates and surfactant solutions. Langmuir 26, 18119–18124. https://doi.org/10.1021/la103193m.

Taylor, C.J., Dieker, L.E., Miller, K.T., et al., 2007. Micromechanical adhesion force measurements between tetrahydrofuran hydrate particles. J. Colloid Interface Sci. 306, 255–261. https://doi.org/10.1016/j.jcis.2006.10.078.

Wang, S.L., Fan, S.S., Lang, X.M., et al., 2020. Particle size dependence of clathrate hydrate particle cohesion in liquid/gaseous hydrocarbons. Fuel 259, 116201–116208. https://doi.org/10.1016/j.fuel.2019.116201.

Yang, S., Kleehammer, D.M., Huo, Z.X., et al., 2004. Temperature dependence of particle-particle adherence forces in ice and clathrate hydrates. J. Colloid Interface Sci. 277, 335–341. https://doi.org/10.1016/j.jcis.2004.04.049.

Yu, Y.J., Luo, Q., Ning, F.L., 2021. Direct measurement of the interaction forces between sediment particles in gas hydrate reservoirs. J. China Univ. Petrol. (Edit. Nat. Sci.) 45, 87–93. https://doi.org/10.3969/j.issn.1673-5005.2021.01.001 (in Chinese).

Zeppieri, S., Rodríguez, J., Ramos, A.L.L.d., 2001. Interfacial tension of alkane + water systems. J. Chem. Eng. Data 46, 1086–1088.